The effect of prolonged irradiation on defect production and ordering in Fe–Cr and Fe–Ni alloys

2011 J. Phys.: Condens. Matter 23 355007

(http://iopscience.iop.org/0953-8984/23/35/355007)

IOP PUBLISHING JOURNAL OF PHYSICS: CONDENSED MATTER

J. Phys.: Condens. Matter **23** (2011) 355007 (13pp) doi:10.1088/0953-8984/23/35/355007

The effect of prolonged irradiation on defect production and ordering in Fe–Cr and Fe–Ni alloys

K Vörtler[1], N Juslin[1,2], G Bonny[3], L Malerba[3] and K Nordlund[1]

[1] Association EURATOM-Tekes, Department of Physics, University of Helsinki, PO Box 43, FIN-00014, Finland
[2] Department of Nuclear Engineering, University of Tennessee, 315 Pasqua Engineering Building, Knoxville, TN 37996, USA
[3] SCK·CEN, Belgian Nuclear Research Centre, Boeretang 200, B-2400 Mol, Belgium

E-mail: katharina.vortler@helsinki.fi

Received 20 May 2011, in final form 12 July 2011
Published 16 August 2011
Online at stacks.iop.org/JPhysCM/23/355007

Abstract

The understanding of the primary radiation damage in Fe-based alloys is of interest for the use of advanced steels in future fusion and fission reactors. In this work Fe–Cr alloys (with 5, 6.25, 10 and 15% Cr content) and Fe–Ni alloys (with 10, 40, 50 and 75% Ni content) were used as model materials for studying the features of steels from a radiation damage perspective. The effect of prolonged irradiation (neglecting diffusion), i.e. the overlapping of single 5 keV displacement cascade events, was studied by molecular dynamics simulation. Up to 200 single cascades were simulated, randomly induced in sequence in one simulation cell, to study the difference between fcc and bcc lattices, as well as initially ordered and random crystals. With increasing numbers of cascades we observed a saturation of Frenkel pairs in the bcc alloys. In fcc Fe–Ni, in contrast, we saw a continuous accumulation of defects: the growth of stacking-fault tetrahedra and a larger number of self-interstitial atom clusters were seen in contrast to bcc alloys. For all simulations the defect clusters and the short range order parameter were analysed in detail depending on the number of cascades in the crystal. We also report the modification of the repulsive part of the Fe–Ni interaction potential, which was needed to study the non-equilibrium processes.

(Some figures in this article are in colour only in the electronic version)

1. Introduction

For nuclear application in future fission and fusion reactors, ferritic/martensitic (FM) and austenitic steels are promising candidate materials. As a contribution to the understanding of the behaviour of high-Cr FM steels (including reduced activation and oxide-dispersion strengthened) and high-Ni austenitic steels (include stainless and duplex) it is useful to model the properties under irradiation by simpler Fe-based binary alloys: Fe–Cr and Fe–Ni alloys.

Radiation damage by energetic particles (neutrons, electrons, ions) in materials leads to changes in the material properties. The scattering of energetic particles induces atomic collisions that can produce an avalanche of displacements at the atomic level (so-called displacement, or collision cascades). The defects thereby produced evolve by diffusion and are the origin of macroscopic radiation damage effects such as swelling, embrittlement and hardening in steels. The characteristic time and length scales of displacement cascades, too short and small to be easily accessed in experiments, are in turn perfectly suitable for simulation tools like molecular dynamics (MD).

The result of an MD simulation depends on the employed force interaction model, the interatomic potential. When analysing primary defect production and ordering in binary alloys, it is important that the interatomic potential

realistically describes not only point-defect properties, such as the stability and mobility of self-interstitial atoms (SIAs) in different configurations, but also thermodynamic properties of the alloy, for example the heat of mixing. Using potentials with the latter features, single cascades in Fe–Cr alloys have been simulated in earlier works with Cr concentrations from 5–15% [1–3]. For Fe–Ni alloys, a potential able to describe the ferritic and austenitic phases as well as the correct defect properties and phase stability has only recently become available, and has not yet been adapted for cascade simulations, by stiffening the short-distance function [4]. This is done as a prerequisite in the present work.

Previous investigations have been mainly restricted to single-cascade simulations and random Fe–Cr alloys. In the only other overlapping cascade study [5], the energies were lower and significantly fewer overlaps were considered. The main results were that in random Fe–Cr the Cr content has hardly any effect on the production of defects or their clustering compared to pure bcc Fe [1–3]. Analysis of the short range order (SRO) parameter in matrices subjected to single 5 keV cascades have revealed Cr ordering in Fe–5%Cr (negative SRO) and Cr clustering in Fe–15%Cr (positive SRO) alloy [2], as expected for Fe–Cr alloys under equilibrium conditions [6, 7].

The purpose of the present paper is to analyse the effect of prolonged radiation damage (neglecting long term diffusion), i.e. by the overlapping of single cascades, on the production of defects, their clustering and distribution. We aim at investigating whether there is any intrinsic difference between the ferritic and austenitic phases of Fe–Cr and Fe–Ni, and between ordered and random crystals, in terms of accumulation of radiation damage. A further objective is to determine whether the changes in atomic distribution observed in single cascades are also dominated by thermodynamic forces after agglomerations of multiple cascade events. We therefore accumulated up to 200 single cascades of 5 keV in the same cell, one after the other: they were randomly distributed in the simulation cell, allowing overlapping and recombination of single-cascade damage. As bcc cells, random Fe–5%Cr, Fe–10%Cr, Fe–15%Cr, Fe–10%Ni and ordered Fe–6.25%Cr crystals were used. The defect evolution and changes in ordering (SRO parameter) were compared to 5 keV cascade overlaps in random Fe–40%Ni, Fe–50%Ni, Fe–75%Ni and ordered Fe–50%Ni fcc matrices.

For comparison with the results of cascade accumulation, single cascades in 100% Ni and random Fe–40%Ni, Fe–50%Ni and Fe–75%Ni were simulated, as no data were available from previous work for these alloys. An extended defect cluster analysis was performed including structural changes such as stacking-fault tetrahedra (SFT) in fcc matrices. For the cascade simulations in Fe–Ni, the potential presented by Bonny *et al* [4] was modified for high energy collisions. We present the fitting procedure for the repulsive part in appendix A and validate the adapted potential by displacement threshold calculations in appendix B. We used the potential by Olsson *et al* [8] for all simulations in Fe–Cr.

2. Method

All simulations were carried out using the MD code PARCAS [9][4]. As interaction models we used the embedded-atom method [10] (EAM) potentials by Olsson *et al* [8, 11] (the two-band EAM potential fitted to the PAW dataset) and by Bonny *et al* [4] (see also appendix A) for calculations in Fe–Cr and Fe–Ni alloys, respectively.

2.1. Cascade overlapping simulations

As bcc simulation cells (random Fe–5%Cr, Fe–10%Cr, Fe–10%Ni, Fe–15%Cr and ordered Fe–6.25%Cr) we created crystals with 148 176 atoms consisting of 42 unit cells in the [100], [010] and [001] directions. The fcc crystals (random Fe–40%Ni, Fe–50%Ni, Fe–75%Ni and ordered Fe–50%Ni) were cubes of 34 unit cells and 157 216 atoms. For the random cells, Cr or Ni atoms were randomly distributed in the Fe crystals according to the desired concentration. The simulation cell for ordered Fe–6.25%Cr was constructed using supercells of one Cr and 15 Fe atoms in a bcc 16-atom basis [12]. The fcc 4-atom basis of ordered Fe–50%Ni (i.e. the $L1_0$ intermetallic compound) consisted of two Fe and two Ni atoms. Using periodic boundary conditions in three dimensions [13], each simulation cell was relaxed at zero pressure and 300 K utilising Berendsen pressure and temperature control [14]. These cells were the initial inputs for the cascade overlapping simulations. The simulation procedure was as follows:

(1) Before each cascade, the cell was randomly shifted in the [100], [010] and [001] directions in order to achieve a uniformly damaged crystal. Each cascade was initiated by giving a random Fe atom near the centre of the cell, the primary knock-on atom (PKA), a recoil energy of 5 keV in a random direction. This allowed a uniform distribution of damage to be achieved, even though the PKA was chosen always at the centre of the cell to avoid as far as possible interaction with the borders of the cell, where the temperature was scaled (thickness one lattice parameter, Berendsen temperature constant 100.0 fs). The simulation time for each cascade run was 20 ps. No electronic stopping was used to be consistent with previous works [1–3]. No maximum energy of border atoms was employed as in single cascades [1–3], i.e. cascade crossing through the cell borders was allowed, though avoided as much as possible.

(2) After each cascade run the atoms were shifted back over the periodic boundaries to keep the cell centred at the origin in order to allow analysis, which uses as a reference the original location of the box. The cell was analysed for defects and ordering (see section 2.3).

(3) In order to take stress out of the system after the cascade, a relaxation run was carried out for 6 ps using pressure

[4] The main principles of the molecular dynamics algorithms are presented in [33, 34]. The adaptive time step and electronic stopping algorithms are the same as in [35].

and temperature control (Berendsen constant 500.0 fs and 100.0 fs, respectively) to 0 pressure and 300 K using a quenching rate of 0.5 K fs^{-1}.

(4) Using the relaxed simulation cell, step (1) was repeated for the next cascade (overlap). We simulated up to 200 cascades in each considered cell.

2.2. 20 keV single cascades in Ni and Fe–Ni alloys

Single cascades with $E_{PKA} = 20$ keV in fcc pure Ni and random Fe–40%Ni, Fe–50%Ni and Fe–75%Ni were simulated following the same procedure as in [1, 2]. The size of the cell was 629 856 atoms (54 unit cells in the [100], [010] and [001] directions) and the crystal structure was equilibrated at 300 K. The simulation time for each single cascade event was 25 ps. We performed 15 events with random PKA angles for each Ni or Fe–Ni crystal. The PKA was Fe for Fe–Ni, and Ni for 100% Ni matrices.

2.3. Analysis

The defect production in bcc cells was analysed using Wigner–Seitz (WS) cells centred at each lattice site: an empty cell corresponded to a vacancy and a cell filled with two atoms to an SIA configuration. For the defects detected by WS cells a cluster connectivity analysis was carried out using second-nearest-neighbour (nn) distances for vacancies and third-nn ones for SIAs. Furthermore, the number of Cr or Ni atoms in SIA positions and in SIA clusters containing at least five defects were counted.

Since a WS cell analysis cannot detect structural changes (e.g. SFTs) and can give an inconsistent number of Frenkel pairs (FPs) at elevated temperatures in fcc structures, a different method was used in fcc cells. Equivalent sphere (ES) analysis was used in fcc crystals following the same approach as in [15]. Atoms were considered 'outside spheres' if they were outside a radius of $r = 0.27a_0$. A cluster analysis of both empty spheres and atoms outside spheres was performed using the first-nearest-neighbour (nn) distance. Vacancies and SIAs were detected by calculating the imbalance of empty spheres and atoms outside spheres belonging to the same cluster, i.e. a cluster consisting of 15 atoms outside spheres and 10 empty spheres was counted as five SIAs. Thus, the number of vacancies is not the number of empty spheres, and the number of SIAs is not the number of atoms outside spheres. It was checked that the number of vacancies was equal to the number of SIAs (which was the number of FPs). SFTs were detected by visually checking for tetrahedral pyramids of empty spheres (i.e. SFTs are not clusters of vacancies). As stacking-fault planes we considered SFT-like planes of empty spheres. Moreover, the number of Ni atoms in atoms outside spheres was counted.

For both fcc and bcc cells a size distribution of the SIA clusters was obtained.

The SRO parameter [16] ($\alpha^{(i)}_{Cr/Ni}$) of the ith nearest-neighbour (nn) shell for Cr or Ni was calculated up to the fifth-nn shell. For bcc a weighted SRO parameter of the first- and second-nn shell (SRO_{12}), as well as of the fourth-

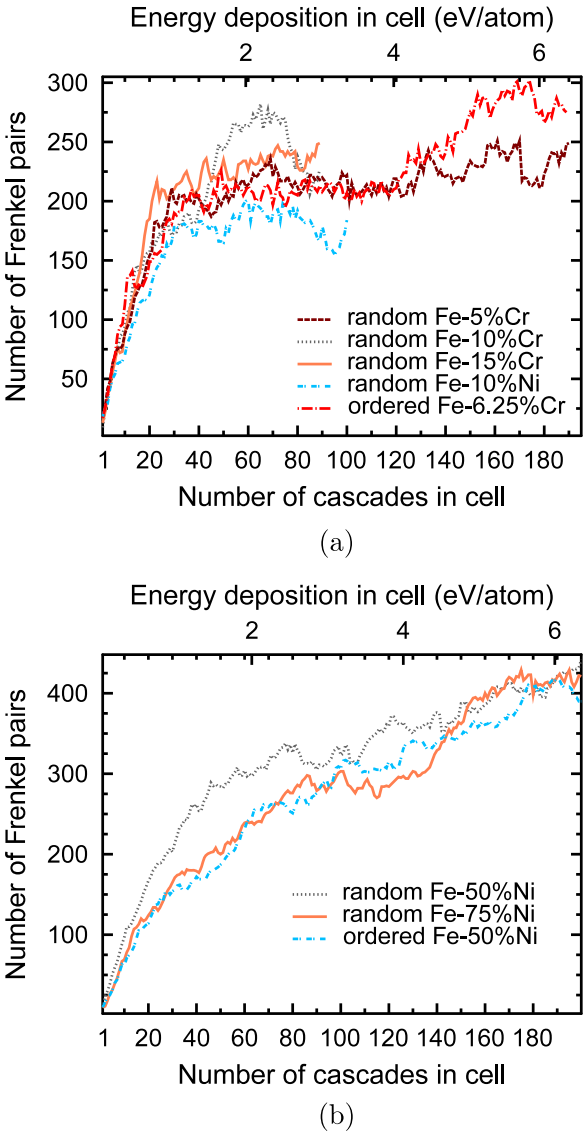

Figure 1. The number of Frenkel pairs depending on the number of cascades in the (a) bcc (WS analysis) and (b) fcc cells (ES analysis).

and fifth-nn shells (SRO_{45}), were introduced, since first- and second-, and fourth- and fifth-nn atoms are very close to each other in bcc:

$$SRO_{12} = \frac{8\alpha^{(1)}_{Cr/Ni} + 6\alpha^{(2)}_{Cr/Ni}}{14}, \quad (1)$$

$$SRO_{45} = \frac{16\alpha^{(4)}_{Cr/Ni} + 8\alpha^{(5)}_{Cr/Ni}}{24}. \quad (2)$$

3. Results and discussion

3.1. Frenkel pair production and structural changes

The number of FPs versus number of cascade overlaps are given in figure 1. Figure 1(a) shows that for all bcc cells a saturation in the number of FPs in the cell appears

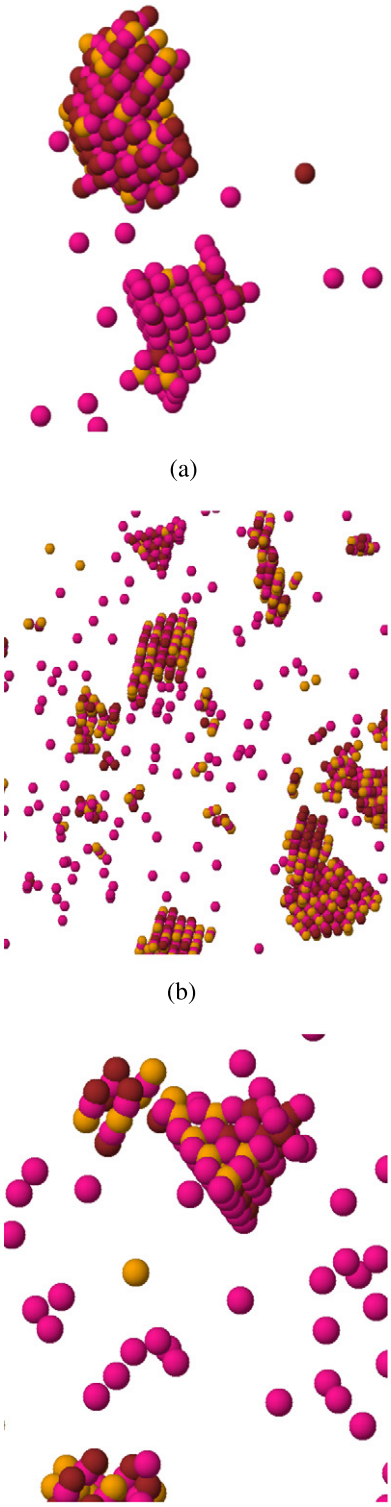

Figure 2. SFT by (a) single 20 keV cascade in Fe–75%Ni, (b) after 64 overlaps in random Fe–50%Ni and (c) after 160 overlaps in ordered Fe–50%Ni. Colour code: magenta (light grey) spheres represent empty spheres, dark red (dark grey) spheres Ni atoms and beige (very light grey) spheres Fe atoms.

by increasing numbers of cascade overlaps (it saturates to roughly 200 FPs for the Fe–Cr cells, while in Fe–10%Ni to a little lower value). Hardly any difference in the FP production

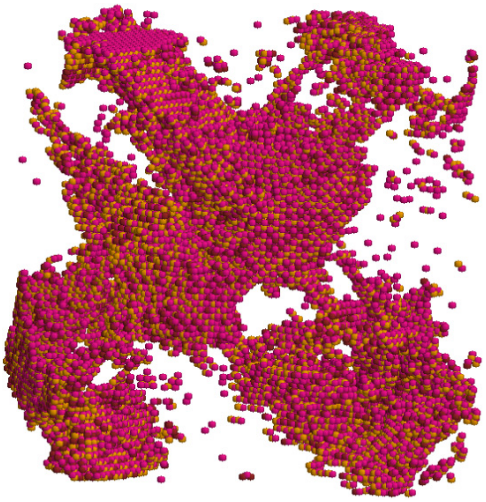

Figure 3. Empty and displaced spheres of run 124 of Fe–40%Ni. Colour code: magenta (light grey) spheres represent empty spheres, dark red (dark grey) spheres Ni atoms and beige (very light grey) spheres Fe atoms.

is seen in ordered Fe–6.25%Cr and random Fe–5%Cr. It is therefore concluded that neither Cr content in the range considered here, nor random or ordered atomic distributions, affect FP production by overlapping cascades. This is the same result as for single cascades in random Fe–Cr, where no difference was seen in the FP production in the Cr concentration range studied here [2].

In the Fe–Ni fcc cells (figure 1(b)), in contrast, no saturation in the number of FPs is observed even after 200 overlaps: FP production somewhat slowed down after about 40 overlaps, but it continues steadily. After about 40 overlaps, there are at least 50% more FPs in fcc crystals than in bcc crystals, although there are only 5% more atoms in the fcc cells. All cells follow a similar trend in the FP production: the number of FPs increases with the number of cascade overlaps, without any effect of ordered atomic distribution or Ni concentration. The number of FPs in single 20 keV cascades in random Fe–Ni and 100% Ni cascades is given in table 1. It can be seen that in Fe–Ni about the same number of FPs are produced in single cascades. In the pure Ni cells the smallest number of FPs is found, although the Ni PKA has a higher mass than the Fe PKA used in the Fe–Ni cells.

During the simulations, as the number of cascade overlaps increased, SFTs appeared in all fcc cells (examples are displayed in figures 2(b) and (c)). The number of empty spheres and atoms outside spheres was 1800–2600 each in the Fe–Ni cells, i.e. much larger than the number of FPs. Moreover, we also observed SFTs in the single 20 keV cascade simulations (figure 2(a)). They were found in all cells in most events, but only in one event in Fe–40%Ni.

In Fe–40%Ni a phase transformation from fcc to bcc in parts of the simulation cell was observed for increasing numbers of cascades in the cell, consistently with the phase diagram predicted by the potential [4]. Therefore the number of defects is not meaningful and is not given here. Figure 3 shows the empty spheres and atoms outside spheres (about

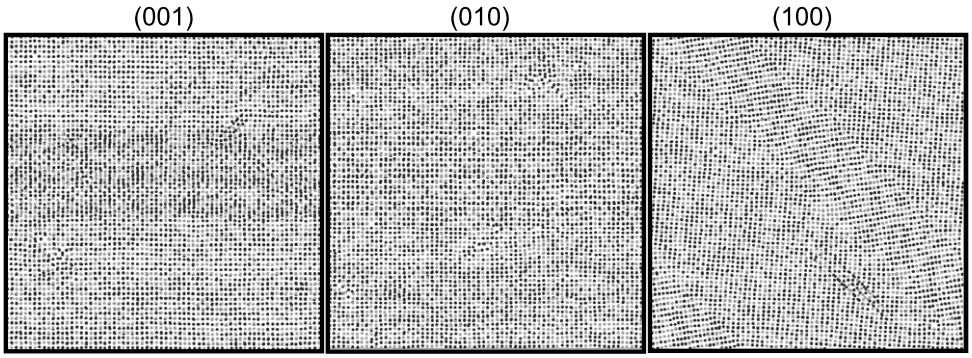

Figure 4. Projection of the final simulation cell of Fe–40%Ni in (001), (010) and (100) planes after run 128. The distortion of the crystal is most evident in the (100) plane. Black dots represent Fe and grey dots Cr atoms.

Table 1. Defect production and their clustering in pure Ni and Fe–Ni crystals by single 20 keV cascades (ES analysis) and $C_{\text{Ni in atoms outside spheres}}/C_{\text{Ni in matrix}}$ is the ratio of Ni in atoms outside spheres over the Ni content in the crystal matrix. Change in short range ordering by the SRO parameter for all atoms in the crystals. The standard 1σ error of the average is given.

	Fe–40%Ni	Fe–50%Ni	Fe–75%Ni	100% Ni
Number of FPs	48 ± 5	39 ± 3	42 ± 3	32 ± 2
SIA clustered fraction (%)	80 ± 3	76 ± 2	80 ± 3	69 ± 3
Vacancy clustered fraction (%)	54 ± 5	40 ± 4	53 ± 5	44 ± 6
$C_{\text{Ni in atoms outside spheres}}/C_{\text{Ni in matrix}}$	0.72 ± 0.03	0.86 ± 0.03	1.06 ± 0.02	1
First shell ΔSRO (10^{-4})	2.9 ± 0.3	2.6 ± 0.3	1.5 ± 0.2	
Second shell ΔSRO (10^{-3})	3.43 ± 0.09	2.80 ± 0.09	0.3 ± 0.1	

22 000 each) after 124 overlaps in Fe–40%Ni. Large planes of different crystal directions throughout the whole cell can be seen. Another illustration of the crystal structure in Fe–40%Ni after 128 overlaps is presented in figure 4. It shows a projection of the 3D cell in the (001), (010) and (100) plane. The cell is distorted from the perfect fcc structure, which can be seen in the different crystal grains, especially in the (100) plane. The cell size of the [100] direction increased from initially 120.073 951 to 129.355 500 Å, in the [010] direction from 120.052 518 to 121.874 200 Å, and decreased in the [001] direction from 120.082 319 to 112.298 50 Å. A bond angle distribution and structural factor analysis revealed that most of the cell is distorted fcc. A few atoms of the cell are bcc-oriented, as a weak bcc peak was observed in the bond angle distribution. Moreover, there was an increase in the structure factor near crystallite boundaries. We conclude that the cell is therefore overall in some intermediate structure between fcc and bcc. Fe–40%Ni is a metastable fcc structure in the phase diagram (figure 5 in [4]). The observed phase change is expected, since more and more defects were created by the increasing number of cascades in the cell. That defects and grain boundaries play a role in the fcc to bcc transformation has been shown previously by MD in Fe–40%Ni [17].

3.2. Cluster analysis

The SIA clustered fraction versus number of cascade overlaps is presented in figure 5. The saturation seen in bcc cells (figure 5(a)) is similar to the one for FP in figure 1(a). It is independent of Cr or Ni content and (initially) random or ordered structures. Single-cascade simulations in Fe–Cr indicate that with increasing number of SIA by increasing PKA, more of them are in clusters than in single SIA defects. However, the saturated value of roughly 80% of SIA in clusters was not reached by 50 keV single cascades in Fe–10%Cr [1].

As in bcc, the SIA clustered fraction also increases to a saturated level with increasing number of cascade overlaps in fcc cells (figure 5(b)). However, this value of 90% is larger than in bcc. This demonstrates that less single SIAs are present in fcc than bcc matrices after about 40–60 cascade overlaps. The SIA clustered fraction of single 20 keV cascades in Fe–Ni (table 1) is lower than the saturated one. For both single and agglomerated cascades, the number of SIA in clusters is independent of Ni content and (initially) Ni ordering in the crystals.

Figure 6 shows the vacancy clustered fraction dependence on cascade overlap. One can see that in both bcc (figure 6(a)) and fcc (figure 6(b)) the fraction of vacancies in clusters fluctuates (in bcc from 30 to 60% and fcc from 20 to 50%). No clear saturation is seen, different from the SIA clustered fraction, especially in the fcc crystals. The vacancy clustered fraction in cascade overlap simulations in bcc cells is comparable with the one observed in single cascades in Fe–Cr alloys [2] and in fcc cells with the one of single 20 eV cascades in Fe–Ni in table 1. In single cascades in pure Ni the vacancy clustered fraction varied from 0 to 70% in the single events.

The ratio of Cr or Ni in SIA positions over the Cr or Ni content in bcc matrices depending on cascade overlaps is illustrated in figure 7(a). As can be seen, the ratio saturates to about 2 for Fe–5%Cr, to about 1–1.5 for other

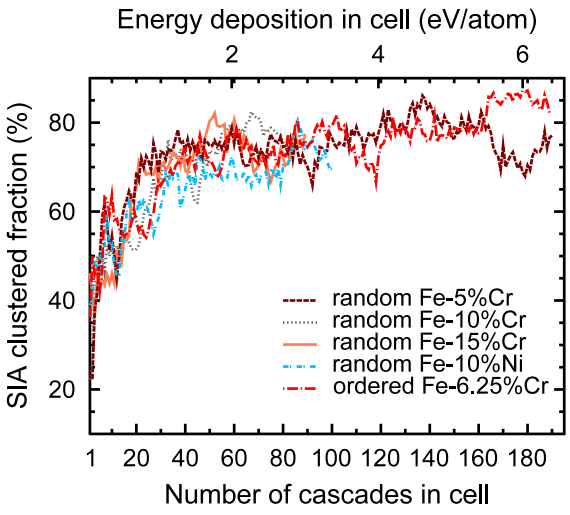

(a)

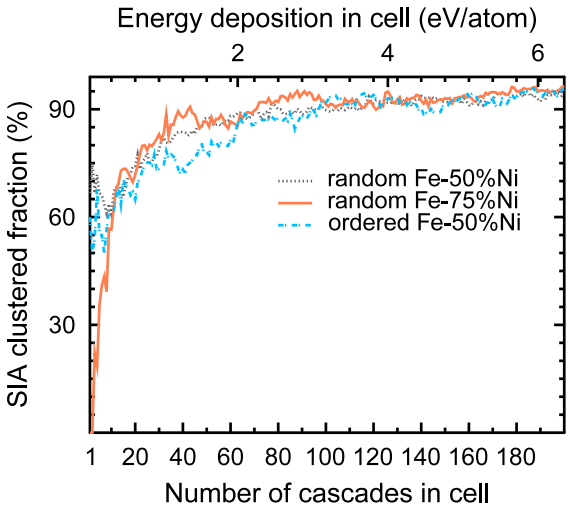

(b)

Figure 5. SIA clustered fraction (%) depending on the number of cascades in (a) bcc and (b) fcc cells.

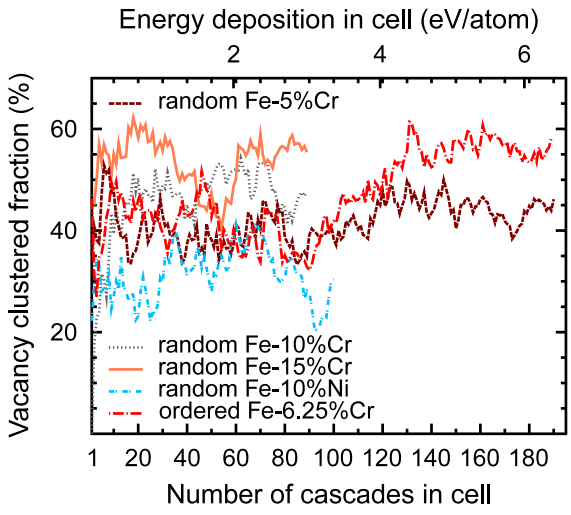

(a)

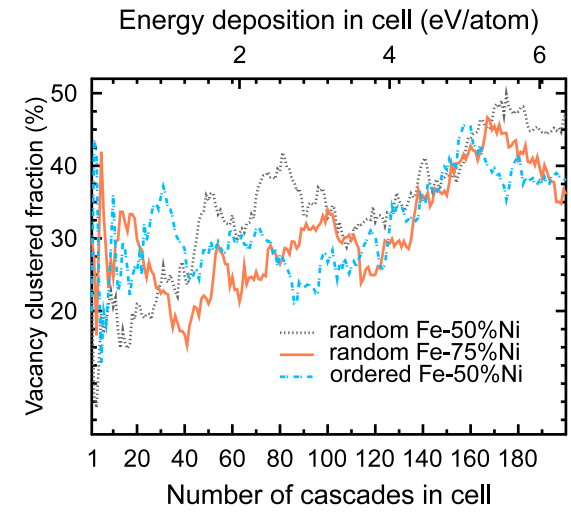

(b)

Figure 6. Vacancy clustered fraction (%) depending on the number of cascades in (a) bcc and (b) fcc cells.

Cr concentrations and 0.8 for Fe–10%Ni. The saturation is similar as for the SIA clustered fraction (figure 5(a)): with increasing numbers of cascades the ratio decreases to about two for Fe–5%Cr (i.e. two times more Cr are in SIA positions than in the matrix), which is slightly smaller than for 5 keV single cascades [2]. The saturated ratio for Fe–5%Cr is smaller than in [5]: however, in the cited work the number of FPs has not yet been saturated. Figure 7(b) shows the ratio of Ni in atoms outside spheres over the Ni content in fcc cells, depending on cascade overlaps. This ratio saturates, similarly to the SIA clustered fraction, for all Fe–Ni crystals to roughly one. The ratio of Ni in atoms outside spheres over the Ni concentration in the matrix for single 20 keV cascades (table 1) is comparable with the ones for 1–10 overlaps in figure 7(b). The trend is similar for both bcc and fcc crystals: when the fraction of SIAs in clusters is saturated; then the Cr or Ni content in SIA positions or in displaced spheres is saturated.

Figure 8 presents the ratio of the Cr or Ni content in large SIA clusters (containing at least five defects) over the Cr or Ni content in bcc cells, versus number of cascade overlaps. As seen, although there are large fluctuations, the ratio is roughly one for all bcc crystals. In single Fe–Cr cascades this ratio had large error bars: however, the saturated ratio of the overlap simulation is about the same [2]. Thus, the enrichment of Cr in SIAs positions in Fe–5%Cr and the depletion of Ni in SIAs positions Fe–10%Ni seen in figure 7(a) is due to small SIA clusters and single SIAs.

The size of the largest SIA cluster increases with increasing number of cascades overlaps as shown in figure 9. As one can see, the growing of SIA clusters by the agglomeration of cascades occurs in both bcc and fcc crystals. Moreover, SIA clusters do not grow ‘linearly’; they can also break up, recombine or become smaller as cascades are overlapping within the cell. For bcc Fe–6.25%Cr after 190 overlaps about 40% of all SIAs are in one large cluster, if

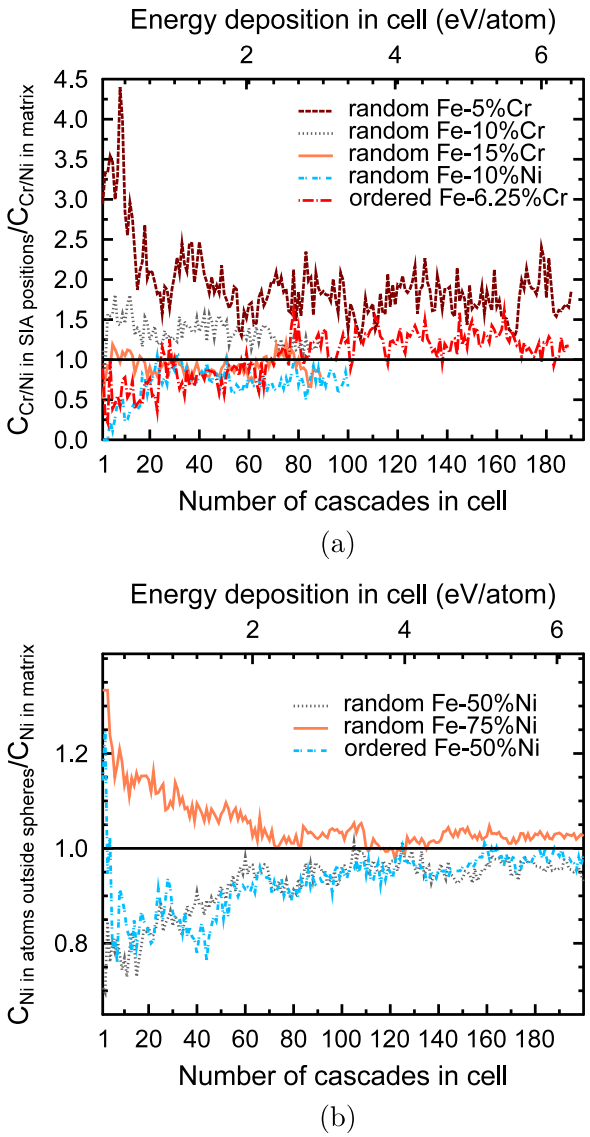

Figure 7. Ratio of Cr or Ni in SIA over the Cr or Ni content in the crystal matrix in (a) bcc cells and (b) ratio of Ni in atoms outside spheres over the Ni content in the matrix in fcc cells depending on the number of cascades.

one compares the size in figure 9 with the number of FPs in figure 5(a). No influence of ordering in bcc cells can be seen; however, in ordered Fe–50%Ni the largest SIA cluster is about two to three times as small than in the initially random fcc crystals.

The distributions of SIA clusters in the final simulation cells (after the last cascade overlap) are given in figure 10. Comparing the values of bcc (a) and fcc cells (b) in the figure, one sees that in bcc more small SIA clusters of size 2–5 defects are in the cell than in fcc, although the total number of FPs is lower in bcc crystals than in the fcc ones. A larger number of SIA clusters/loops containing more than five defects was formed in fcc cells during the cascade overlaps. Comparing the SIA cluster distribution of single 20 keV cascades in bcc cells (figure 1 in [3]) with the one

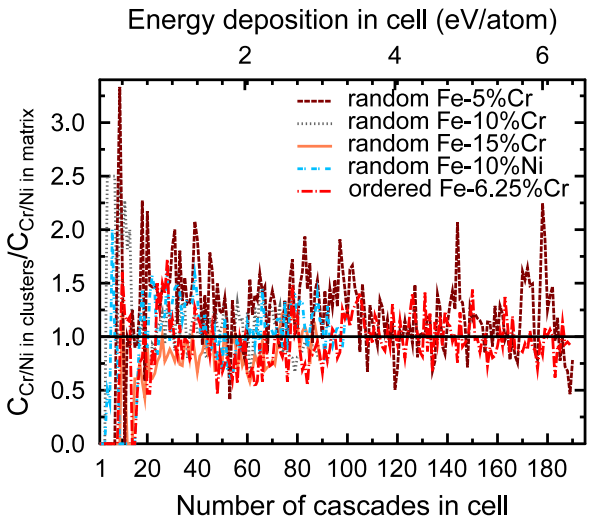

Figure 8. Ratio of Cr or Ni in clusters (containing at least five defects) over the Cr or Ni content in the crystal matrix in (a) bcc and (b) fcc cells.

of single 20 keV cascades in fcc cells (figure 11), no extreme differences can be seen.

3.3. Changes in ordering

Changes in ordering (identified by the SRO parameters in different nn shells) while accumulating cascades in the bcc cells are shown in figure 12. As seen, in Fe–10%Ni the SRO_{12} parameter is increasing (becoming positive with increasing numbers of cascades), and the third-shell SRO and SRO_{45} parameters are about zero: formation of small Ni clusters is observed. The SRO parameters are negative in all shells in Fe–6.25%Cr, denoting the presence of short range ordering. The short range ordering in Fe–6.25%Cr, however, decreases for increasing number of cascade overlaps: the cascades induce some disordering of the Cr atoms in the matrix, perhaps a sign that the stability of the Fe–6.25%Cr ordered structure is limited. In Fe–5%Cr the SRO parameters in all shells are decreasing (becoming more negative) with increasing numbers of cascades: the Cr atoms are thus redistributed within the cell in a way that short range ordering is favoured. In Fe–10%Cr the SRO_{12} parameter is about constant zero, while the third-shell SRO and SRO_{45} parameters are decreasing (becoming negative) with increasing numbers of cascades. In Fe–15%Cr the SRO_{12} parameter is increasing to a positive value and the third-shell SRO and SRO_{45} parameters are decreasing to a negative value. By visual inspection, we saw the formation of small (two to three SIAs) Cr clusters in Fe–10%Cr and Fe–15%Cr. Due to these small Cr clusters, any Cr atom will only see other Cr atoms within the second-nn distance, not further, while the matrix becomes ordered and depleted, which can be seen in the negative third-shell SRO and SRO_{45} parameters. In Fe–10%Cr, the number of clusters is small and the positive values in SRO_{12} are compensated by the negative values (Cr ordering/depletion in the matrix): on average, Cr appears as if it was randomly distributed in the crystal. In Fe–15%Cr Cr

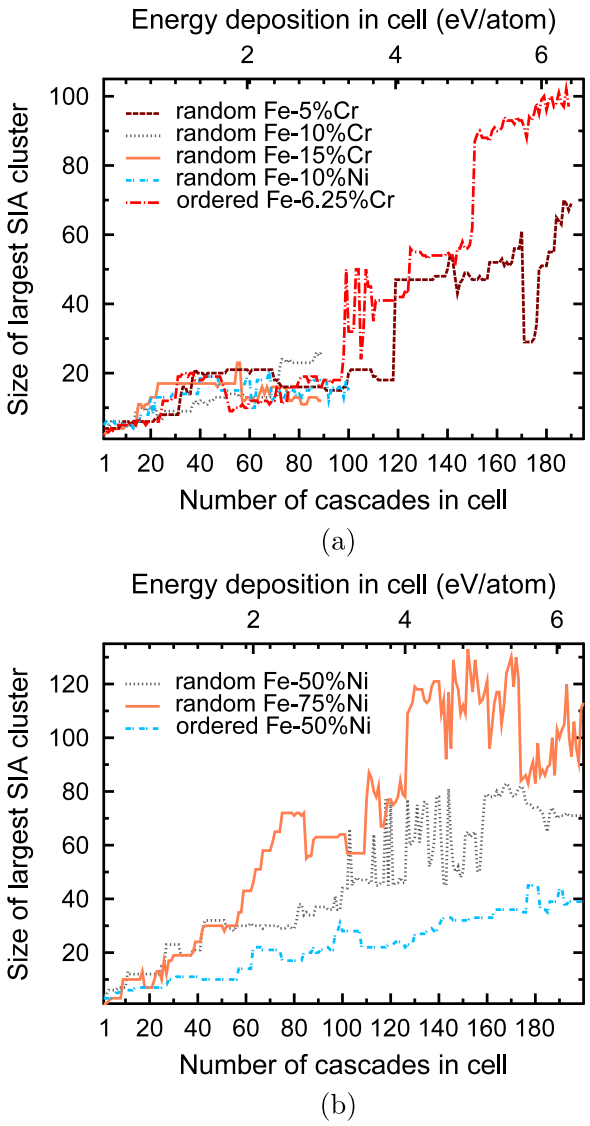

Figure 9. Size of largest SIA cluster depending on the number of cascades in (a) bcc and (b) fcc cells.

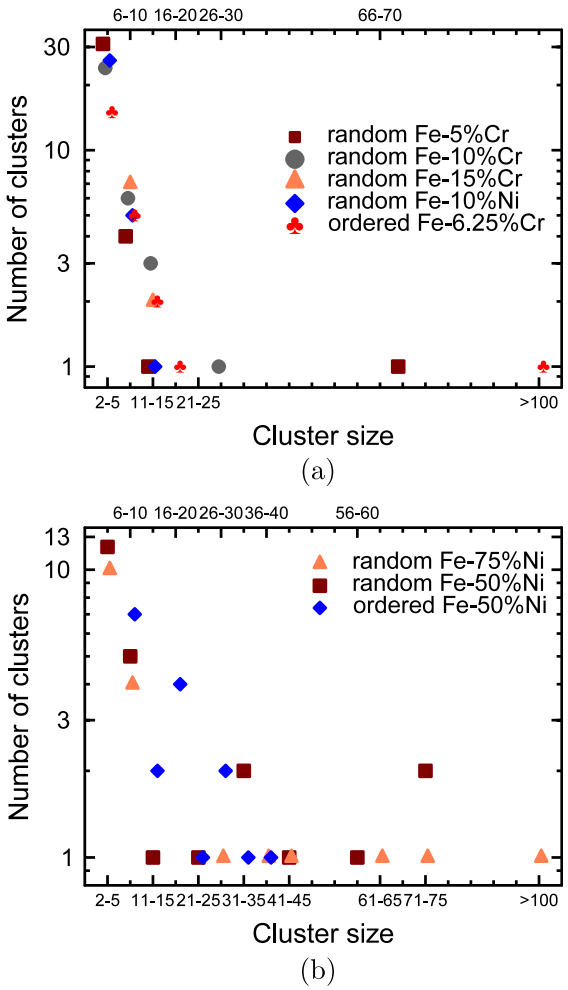

Figure 10. Distribution of SIA cluster of the final simulation cell: (a) bcc and (b) fcc.

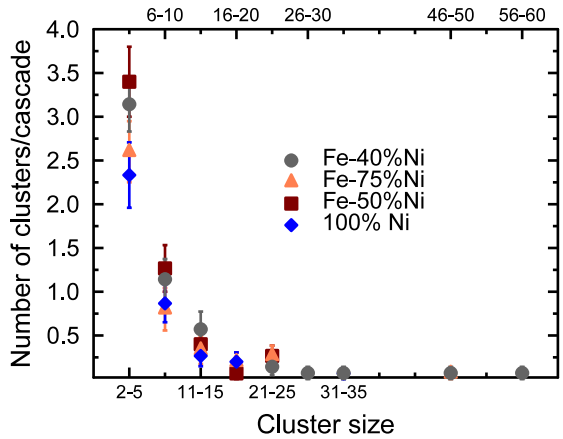

Figure 11. Distribution of SIA clusters by single 20 keV cascades in Ni and Fe–Ni crystals. The 1σ standard error of the average is given.

clustering is more pronounced than Cr ordering/depletion in the matrix: on average there is Cr clustering in the crystal.

The trends observed in initially random Fe–Cr crystals, i.e. Fe–5%Cr becomes more ordered, while in Fe–15%Cr small Cr clusters are formed, and in Fe–10%Cr the alloy stays on average random, agree with the SRO_{12} parameters in single cascades [2]. Moreover, our observations are consistent with the interpretation of the SRO parameter in a solid solution with (forming) Cr precipitates in Fe-rich Fe–Cr alloys [18]. Finally, our results do not contradict the experimentally measured SRO parameters of equilibrium alloys [6, 7]. Unfortunately, though, direct comparison with the experiments in [6, 7] is not possible, since the conditions are largely different: here we produced atomic redistribution by accumulating damage in a diffusionless system, while there this was achieved by aging and, in addition, no guarantee exists that thermodynamic equilibrium was finally reached.

The first- to fifth-nn shell SRO parameter in fcc cells is shown in figure 13. The SRO parameter is switching signs in the initially ordered Fe–50%Ni alloy: initially long range ordering is present. This long range order is broken and the alloy is being disordered with increasing numbers of cascades in the cell, since all SRO shells converge to zero.

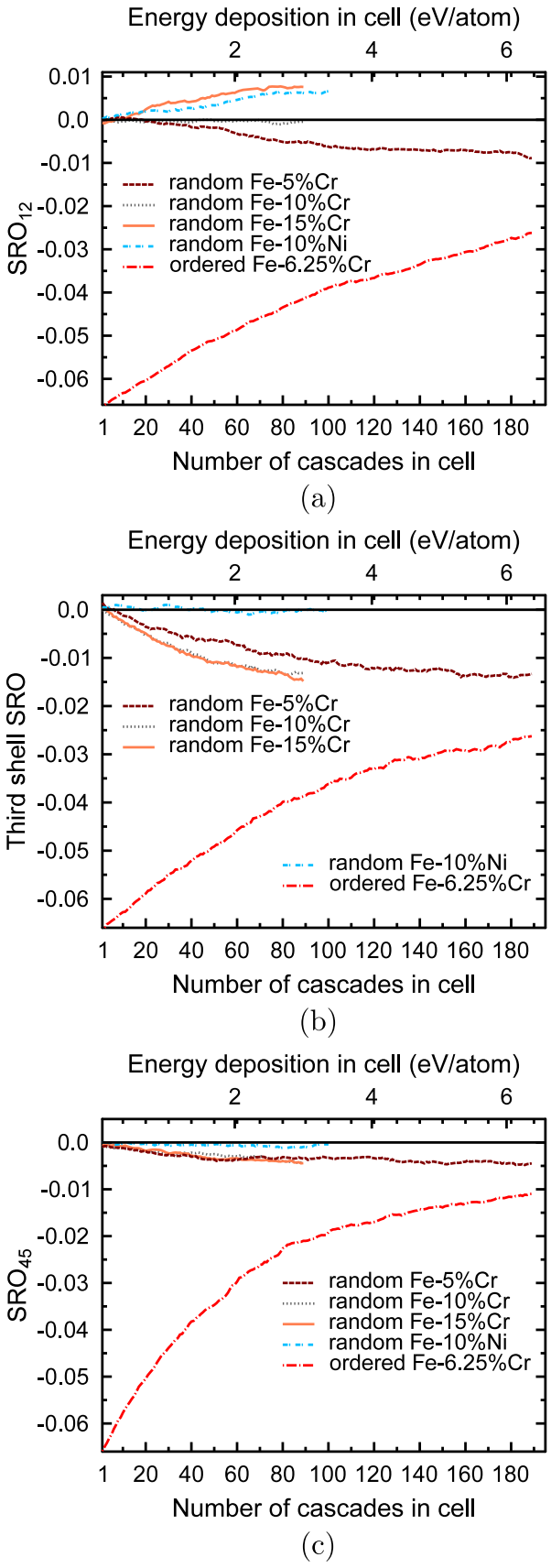

Figure 12. The change in ordering depending on the number of cascades in bcc cells by (a) the average SRO parameter of first- and second-, (b) SRO parameter of third-, and (c) in the average SRO of fourth- and fifth-nn shell.

The SRO parameters of all nn shells are close to zero in the initially random Fe–Ni alloys. We therefore conclude that one cannot tell if there is a tendency towards Ni ordering or clustering in the initially random alloys. To obtain a reliable conclusion more statistics, e.g. by running simulations in initially different random cells, would be needed, which is beyond the scope of this work.

Our simulation of cascades in ordered matrices agree with other studies: disordering in initially ordered fcc cells was also observed in Ni–Al alloys (experimentally and by MD) [19, 20].

4. Conclusions

We have studied the overlapping of single-cascade events within one simulation cell of bcc Fe–Cr and Fe–Ni and fcc Fe–Ni alloys of different Ni and Cr concentrations in initially random and ordered Ni and Cr distributed crystals.

One main difference in the FP production by increasing numbers of cascades in the bcc and fcc simulation cells was identified. In bcc cells, a saturation of the number of FPs was seen. In the fcc alloys, the number of FPs was not saturated after 200 cascades and more damage was accumulated in the fcc crystals than in the bcc ones. We conclude that more efficient growth of SIA clusters and SFTs in fcc alloys are responsible for the higher damage accumulation. Although the results of this work are without long timescale diffusion effects, the experimental trend of more loops in fcc than in bcc metals is reproduced [21]. Our results confirm that bcc materials are more 'radiation resistant' than fcc ones and are therefore more suitable for nuclear applications from this perspective.

As already mentioned, we did not take diffusion processes into account in our simulation. Therefore, our results are important since they show that the high temperature and possibly the local melting induced by the heat spike of cascades and their agglomeration (in the short time scales) is enough to form small Cr clusters in Fe–15%Cr, and produce Cr ordering in Fe–5%Cr in initially random crystals. The effect of the production of small Cr clusters and Cr ordering is cancelled in Fe–10%Cr, which suggests that, at least from the point of view of phase stability, this concentration may present advantages for nuclear applications.

Acknowledgments

This work, supported by the European Communities under the Contract of Association between EURATOM/Tekes, was carried out within the framework of the European Fusion Development Agreement. This research has also received partial funding from EURATOM's 7th Framework Programme (FP7/2007–2011), under grant agreement no. 212175 (GetMat project) and partially contributes to the Perform60 project. It was performed within the Finnish Centre of Excellence in Computational Molecular Science (CMS), financed by the Academy of Finland and the University of Helsinki. The authors thank F Soisson, M Hou and C Becquart for fruitful discussion.

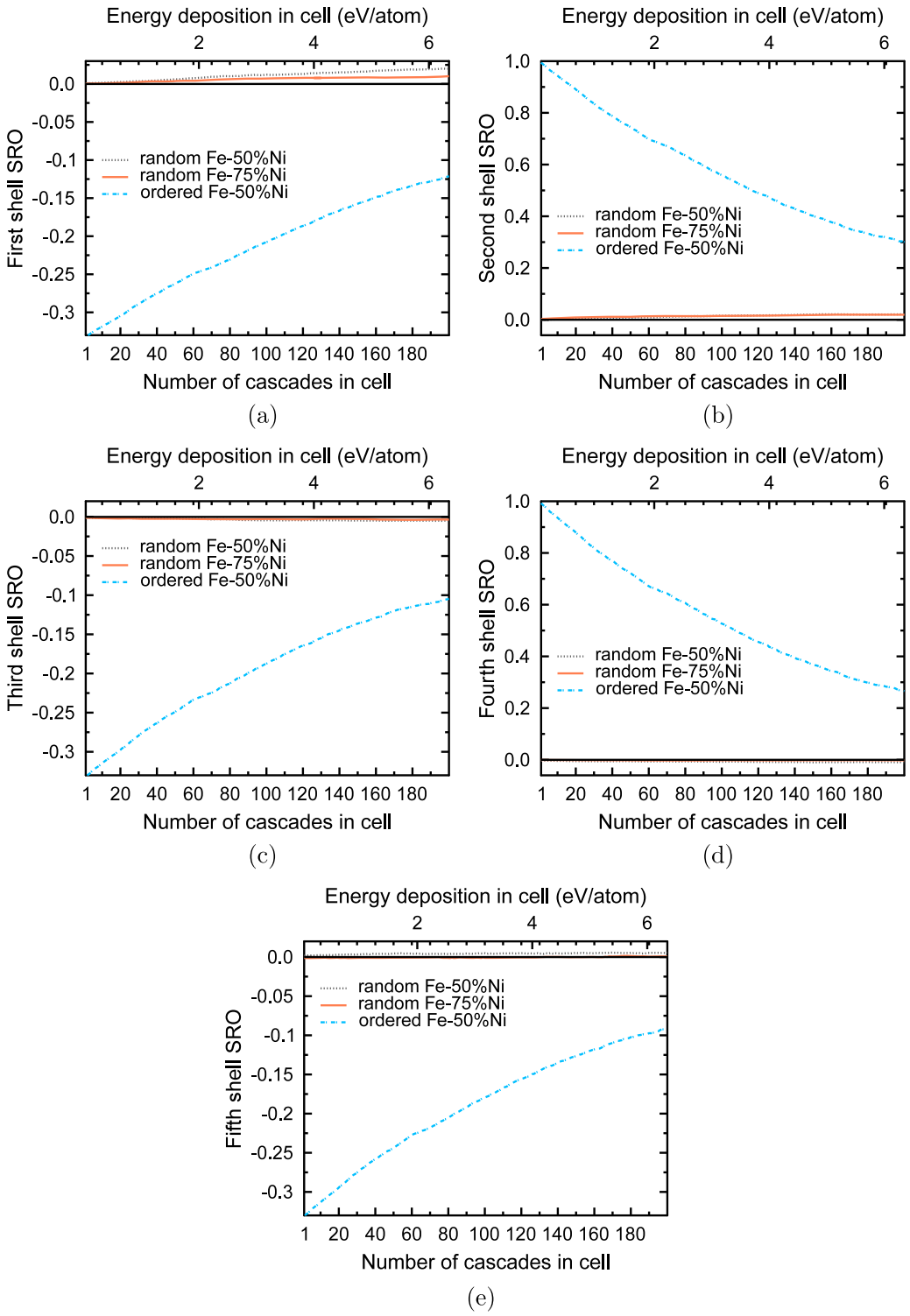

Figure 13. First- to fifth-shell SRO parameter depending on the number of cascade in fcc cells.

Appendix A. Repulsive potential fitting for Fe–Ni

The original equilibrium potentials for the Fe–Ni system by Bonny *et al* include an own Fe–Ni EAM pair potential [4] and the transformed original Ni (Voter–Chen [22]) and Fe ('Mendelev 2' [23]) potentials. The original Fe–Fe interactions include a well-tested repulsive part and were therefore not changed. To describe the Ni–Ni and Fe–Ni repulsive interactions, the corresponding Ziegler–Biersack–Littmark (ZBL) repulsive potentials [24] were transformed as in [4]. Moreover, the transformed ZBL potential for Ni–Ni was lowered by 50 eV.

The fitting formalism of the EAM pair potentials for Ni–Ni and Fe–Ni is as for the Dudarev–Derlet DD–BN potential in [25]. In short, the modified EAM pair potential is constructed by taking the (transformed and possibly lowered)

Table A.1. Polynomial parameters a_n of the potential $V_{\text{int}} = p_{\text{int}}$ (equation (A.1)) between $r_1 = 1.050\,56$ and $r_2 = 1.850\,24$ for Ni–Ni, Fe–Ni EAM pair potentials and EAM electron density of Ni.

	Ni–Ni	Fe–Ni	ρ_{Ni}
a_0	$7.641\,109\,229\,831\,62 \times 10^1$	$-3.915\,217\,865\,167\,98 \times 10^2$	$2.248\,100\,044\,641\,12 \times 10^0$
a_1	$-2.980\,023\,412\,308\,81 \times 10^2$	$3.179\,945\,287\,274\,60 \times 10^3$	$-1.554\,255\,876\,037\,20 \times 10^1$
a_2	$-2.720\,523\,756\,503\,84 \times 10^2$	$-1.034\,647\,953\,877\,89 \times 10^4$	$4.188\,572\,576\,821\,180 \times 10^1$
a_3	$2.822\,263\,103\,857\,06 \times 10^3$	$1.695\,391\,344\,612\,59 \times 10^4$	$-5.515\,291\,011\,218\,82 \times 10^1$
a_4	$-4.590\,735\,459\,934\,82 \times 10^3$	$-1.412\,066\,490\,506\,21 \times 10^4$	$3.559\,099\,462\,731\,22 \times 10^1$
a_5	$2.393\,430\,349\,518\,32 \times 10^3$	$4.847\,163\,566\,261\,18 \times 10^3$	$-8.729\,555\,576\,066\,40 \times 10^0$

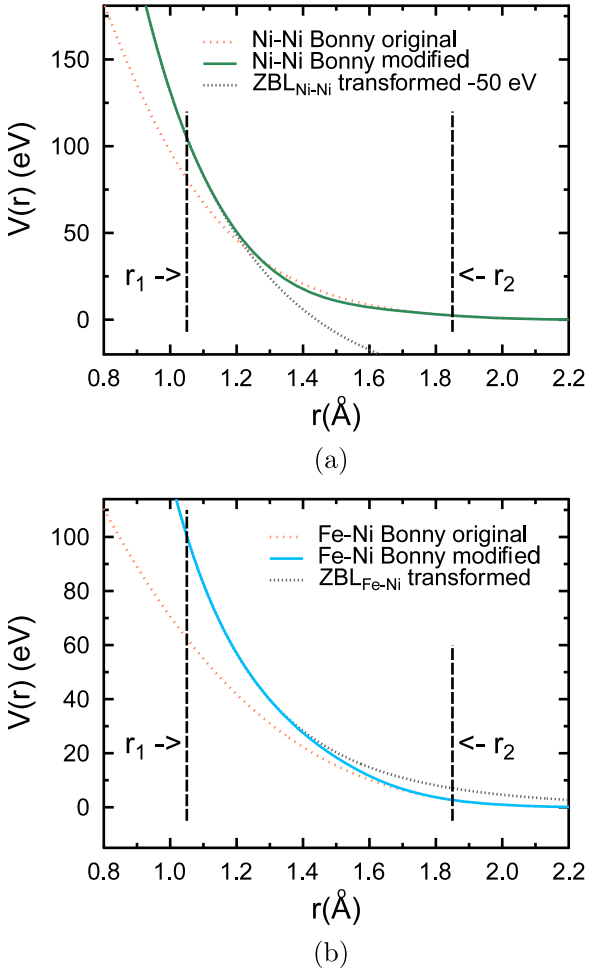

Figure A.1. Modified (a) Ni–Ni and (b) Fe–Ni potentials. The transformed ZBL repulsive potential (minus 50 eV for Ni–Ni in (a)) was fitted to the original potential by Bonny *et al* [4] from the atomic distances r_1 to r_2. The original Ni–Ni potential by Bonny in (a) is the transformed Ni potential by Voter and Chen [22].

ZBL repulsive potential for atomic distances smaller than r_1, the equilibrium EAM pair potential for distances larger than r_2 and joining the two parts using the interpolating polynomial

$$p_{\text{int}} = a_0 r^5 + a_1 r^4 + a_2 r^3 + a_3 r^2 + a_4 r + a_5, \quad \text{(A.1)}$$

where a_n are the polynomial parameters. For both Ni–Ni and Fe–Ni we used $r_1 = 1.050\,56$ and $r_2 = 1.850\,24$. The modified pair potentials are shown in figure A.1 and the corresponding a_n are given in table A.1.

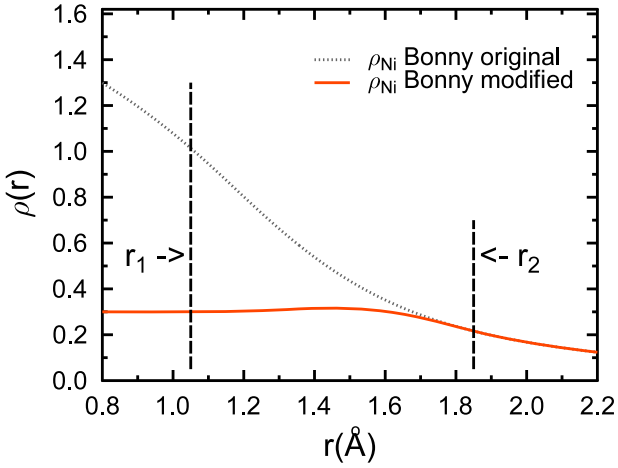

Figure A.2. Modification of the Ni electron density ρ_{Ni}. The constant 0.3 was fitted from the atomic distances r_1 to r_2 on the original density by Bonny *et al* [4] that is the transformed Ni electron density by Voter and Chen [22].

In addition, the EAM electron density for Ni was modified to avoid a double representation of the repulsive interactions [10]. The modified Ni EAM electron density was set to $\rho_C^{\text{Ni}} = 0.3$ for distances smaller than r_1, the original (transformed) density for distances larger than r_2 and for values in between by a fitted polynomial of the form in equation (A.1). Figure A.2 shows the modified Ni electron density; fitting parameters a_n are given in table A.1.

The whole modified potential set can be found at http://www.ctcms.nist.gov/potentials/Fe-Ni.html.

Appendix B. Displacement threshold calculations in Fe–Ni

The method for calculating displacement threshold energies is described in detail elsewhere [26]. The threshold energy $E_D(\theta, \phi)$ is calculated in a random direction for a random or specific atom in the simulation cell. The energy was raised in 2 eV steps for each specific direction (±1 eV uncertainty). We calculated the average displacement threshold energy:

$$E_{d,\text{ave}}^{\text{av}} = \frac{\int_0^{2\pi}\int_0^{\pi} E_d(\theta,\phi)\sin\theta\,\mathrm{d}\theta\,\mathrm{d}\phi}{\int_0^{2\pi}\int_0^{\pi}\sin\theta\,\mathrm{d}\theta\,\mathrm{d}\phi} \quad \text{(B.1)}$$

over all directions (angles). The average over the specific [100], [110] and [111] lattice directions was calculated in the interval Δ0.2 for each Miller index, mimicking

Table B.1. Results of threshold displacement energy calculation in the Fe–Ni system using the modified Ni–Ni and Fe–Ni interactions of this work (Fe–Fe is unmodified). The uncertainty of the direction-specific $E_d(\theta, \phi)$ and medium $E^{\text{av}}_{d,\text{med}}$ thresholds are ±1 eV. The average threshold $E^{\text{av}}_{d,\text{ave}}$ is obtained as in equation (B.1) and $N_{\text{directions}}$ is the number of directions for which a threshold was simulated. The standard 1σ error of the average is given. Fe/Ni (random recoil) means the thresholds were simulated in pure cells and random recoils over one unit cell. For the calculations of a pure Fe cell with an Ni recoil in the centre, Fe–1Ni, Fe–1Fe is a corresponding pure Fe cell using the same recoil position (respectively the same applies for Ni–1Fe and Ni–1Ni).

		$E_d(\theta, \phi)$					
Potential	$N_{\text{directions}}$	All	[100]	[110]	[111]	$E^{\text{av}}_{d,\text{ave}}$	$E^{\text{av}}_{d,\text{med}}$
Ni (random recoil)	1925	30	34	32	48	72.3 ± 0.9	64
Ni experiments[a]		20	38	21	>60	40	
Fe (random recoil)	5046	16	16	30	26	38.1 ± 0.2	36
Fe experiments[b]		16–18	17	>30	20		
Ni–1Fe	3272	32	50	32	76	69.0 ± 0.6	58
Ni–1Ni	5954	30	36	30	48	71.2 ± 0.5	64
Fe–1Ni	2611	22	24	36	32	37.7 ± 0.3	32
Fe–1Fe	3604	16	16	30	32	37.6 ± 0.3	36

[a] References [31, 29, 30].
[b] References [31, 28, 32].

experimental beam spreading. At least about 2000 directions were simulated for each cell.

The bcc simulation cell size was 4608 atoms ($12 \times 12 \times 16$ unit cells) for a pure Fe cell and an Fe cell with one Ni in the centre. The fcc cells (pure Ni and Ni cell with one Fe in the centre) consisted of 5600 atoms ($10 \times 10 \times 14$ unit cells). Employing the modified potentials of appendix A and the unchanged Fe potential into PARCAS, the initial Fe and Fe–Ni cells were thermalised at 36 K (temperature as in [26–28]) or 10 K (Ni cell) as in section 2.

For each threshold energy step and direction, the energy was given to either a random recoil atom in the centre unit cell, or to a specific recoil atom in the centre of the simulation cell. The simulation time was 6 ps. Berendsen temperature control (70.0 fs) at the cell borders of one lattice parameter and no electronic stopping was used. The defect was detected as in section 2 with the addition that the final potential energy of the cell was checked if it was larger than 4 eV of the initial one. If a defect was detected, the threshold energy at this specific direction was considered to be found.

Table B.1 presents the calculated thresholds. The threshold energy of all calculated directions for Ni is by 30 eV too high compared to 20 eV of experiments [29]. Without affecting the equilibrium properties of the Fe–Ni potentials [4], a better Ni–Ni fit was not achieved. The trend of having the highest threshold in [111], the second highest in [100] and third highest in the [110] for Ni is, however, as in the experimental data [30, 29]. The average and medium thresholds for the Ni cell with Fe recoil are lower than in the corresponding Ni cell: however, the specific thresholds of all, [100], [110] and [111] directions are higher. For the Fe cell with Ni recoil, the average threshold is about the same as in the corresponding Fe cell using the same recoil position. However, the thresholds of all [100], [110] and [111] directions are higher and the medium threshold is lower. There is a lack of experimental data for mixed Fe–Ni cells for comparison. However, we consider the threshold energies of the modified potentials reasonable for cascade studies.

References

[1] Björkas C, Nordlund K, Malerba L, Terentyev D and Olsson P 2008 Simulation of displacement cascades in $Fe_{90}Cr_{10}$ using a two band model potential *J. Nucl. Mater.* **372** 312–7

[2] Vörtler K, Björkas C, Terentyev D, Malerba L and Nordlund K 2008 The effect of Cr concentration on radiation damage in Fe–Cr alloys *J. Nucl. Mater.* **382** 24–30

[3] Terentyev D, Vörtler K, Björkas C, Nordlund K and Malerba L 2010 Primary radiation damage in bcc Fe and Fe–Cr crystals containing dislocation loops *J. Nucl. Mater.*

[4] Bonny G, Pasianot R C and Malerba L 2009 Fe–Ni many-body potential for metallurgical applications *Model. Simul. Mater. Sci. Eng.* **17** 025010

[5] Terentyev D, Olsson P, Klaver T P C and Malerba L 2008 On the migration and trapping of single self-interstitial atoms in dilute and concentrated FeCr alloys: atomistic study and comparison with resistivity recovery experiments *Comput. Mater. Sci.* **43** 1183–92

[6] Mirebeau I, Hennion M and Parette G 1984 First measurement of short-range-order inversion as a function of concentration in a transition alloy *Phys. Rev. Lett.* **53** 687–90

[7] Mirebeau I and Parette G 2010 Neutron study of the short range order inversion in $Fe_{1-x}Cr_x$ *Phys. Rev.* B **82** 104203

[8] Olsson P, Wallenius J, Domain C, Nordlund K and Malerba L 2005 Two-band model of α-prime phase formation in Fe–Cr *Phys. Rev.* B **72** 214119

[9] Nordlund K 2006 PARCAS computer code

[10] Daw M S, Foiles S M and Baskes M I 1993 The embedded-atom method: a review of theory and applications *Mater. Sci. Rep.* **9** 251

[11] Olsson P, Wallenius J, Domain C, Nordlund K and Malerba L 2006 Erratum: two-band modeling of α-prime phase formation in Fe–Cr [*Phys. Rev.* b **72** 214119 (2005)] *Phys. Rev.* B **74** 229906

[12] Nguyen-Manh D, Lavrentiev M Y and Dudarev S L 2008 The Fe–Cr system: atomistic modelling of thermodynamics and kinetics of phase transformations *C.R. Phys.* **9** 379–88

[13] Allen M P and Tildesley D J 1989 *Computer Simulation of Liquids* (Oxford: Oxford University Press)

[14] Berendsen H J C, Postma J P M, van Gunsteren W F, DiNola A and Haak J R 1984 Molecular dynamics with coupling to external bath *J. Chem. Phys.* **81** 3684

[15] Voskoboinikov R E, Osetsky Yu N and Bacon D J 2008 Computer simulation of primary damage creation in displacement cascades in copper. I. Defect creation and cluster statistics *J. Nucl. Mater.* **377** 385–95

[16] Cowley J M 1950 An approximate theory of order in alloys *Phys. Rev.* **77** 669–75
[17] Grujicic M and Dang P 1995 Computer simulation of martensitic transformation in Fe–Ni face-centered cubic alloys *Mater. Sci. Eng.* A **201** 194–204
[18] Erhart P, Caro A, Serrano de Caro M and Sadigh B 2008 Short-range order and precipitation in Fe-rich Fe–Cr alloys: atomistic off-lattice Monte Carlo simulations *Phys. Rev.* B **77** 134206
[19] Abromeit C, Wollenberger H, Matsumura S and Kinoshita C 2000 Stability of ordered phases under irradiation *J. Nucl. Mater.* **276** 104–13
[20] Schmitz G, Ewert J C, Harbsmeier F, Uhrmacher M and Haider F 2001 Phase stability of decomposed Ni–Al alloys under ion irradiation *Phys. Rev.* B **63** 224113
[21] Singh B N and Evans J H 1995 Significant differences in defect accumulation behaviour between fcc and bcc crystals under cascade damage conditions *J. Nucl. Mater.* **226** 277–85
[22] Voter A and Chen S P 1989 Accurate interatomic potentials for Ni, Al and Ni_3Al *Mater. Res. Soc. Symp. Proc.* **82** 175
[23] Mendelev M I, Han S, Srolovitz D J, Ackland G J, Sun D Y and Asta M 2003 Development of new interatomic potentials appropriate for crystalline and liquid iron *Phil. Mag.* **83** 3977–94
[24] Ziegler J F, Biersack J P and Littmark U 1985 *The Stopping and Range of Ions in Matter* (New York: Pergamon)
[25] Björkas C and Nordlund K 2007 Comparative study of cascade damage in Fe simulated with recent potentials *Nucl. Instrum. Methods Phys. Res.* B **259** 853
[26] Nordlund K, Wallenius J and Malerba L 2006 Molecular dynamics simulations of threshold energies in Fe *Nucl. Instrum. Methods Phys. Res.* B **246** 322–32
[27] Juslin N, Nordlund K, Wallenius J and Malerba L 2007 Simulation of threshold displacement energies in FeCr *Nucl. Instrum. Methods Phys. Res.* B **255** 75
[28] Maury F, Biget M, Vajda P, Lucasson A and Lucasson P 1976 Anisotropy of defect creation in electron-irradiated iron crystals *Phys. Rev.* B **14** 5303
[29] *Neutron Radiation Damage Simulation by Charged Particle Simulation* Rep. No. ASTM E 521-77
[30] Bourret A 1971 Irradiation damage in nickel and iron in a high-voltage electron microscope and threshold energy determination *Phys. Status Solidi* a **4** 813–25
[31] Lucasson P G and Walker R M 1962 Production and recovery of electron-induced radiation damage in a number of metals *Phys. Rev.* **127** 485
[32] Lomer J N and Pepper M 1967 Anisotropy of defect production in electron irradiated iron *Phil. Mag.* **16** 119
[33] Nordlund K, Ghaly M, Averback R S, Caturla M, Diaz de la Rubia T and Tarus J 1998 Defect production in collision cascades in elemental semiconductors and fcc metals *Phys. Rev.* B **57** 7556–70
[34] Ghaly M, Nordlund K and Averback R S 1999 Molecular dynamics investigations of surface damage produced by keV self-bombardment of solids *Phil. Mag.* A **79** 795
[35] Nordlund K 1995 Molecular dynamics simulation of ion ranges in the 1–100 keV energy range *Comput. Mater. Sci.* **3** 448